Journal of the Chinese Institute of Engineers

ISSN: 0253-3839 (Print) 2158-7299 (Online) Journal homepage: http://www.tandfonline.com/loi/tcie20

Prediction of silicon dry etching using a piecewise linear algorithm

V.M. Jimenez-Fernandez , C. Reyes-Betanzo , M. Angelica-Cerdan , Z.J. Hernandez-Paxtian , H. Vazquez-Leal & A. Itzmoyotl-Toxqui

To cite this article: V.M. Jimenez-Fernandez , C. Reyes-Betanzo , M. Angelica-Cerdan , Z.J. Hernandez-Paxtian , H. Vazquez-Leal & A. Itzmoyotl-Toxqui (2013) Prediction of silicon dry etching using a piecewise linear algorithm, Journal of the Chinese Institute of Engineers, 36:7, 941-950, DOI: 10.1080/02533839.2012.743231

To link to this article: https://doi.org/10.1080/02533839.2012.743231

Published online: 15 Apr 2013.

Submit your article to this journal

Article views: 59

Citing articles: 2 View citing articles

Full Terms & Conditions of access and use can be found at
http://www.tandfonline.com/action/journalInformation?journalCode=tcie20

Journal of the Chinese Institute of Engineers, 2013
Vol. 36, No. 7, 941–950, http://dx.doi.org/10.1080/02533839.2012.743231

Taylor & Francis
Taylor & Francis Group

Prediction of silicon dry etching using a piecewise linear algorithm

V.M. Jimenez-Fernandez[a]*, C. Reyes-Betanzo[b], M. Angelica-Cerdan[c], Z.J. Hernandez-Paxtian[d], H. Vazquez-Leal[a] and A. Itzmoyotl-Toxqui[b]

[a]*Facultad de Instrumentación Electrónica y Ciencias Atmosféricas, Universidad Veracruzana, Circuito Gonzalo Aguirre Beltrán s/n, Zona Universitaria, 91000, Xalapa, Veracruz, México;* [b]*Electronics Department, National Institute for Astrophysics, Optics and Electronics (INAOE), Luis Enrique Erro No. 1, Tonantzintla, 72840, Puebla, México;* [c]*Departamento de Electrónica, Instituto Tecnológico Superior de Xalapa, Sección 5A Reserva Territorial s/n, Santa Bárbara, 91096, Xalapa, Veracruz, México;* [d]*Instituto de Farmacobiología, Universidad de la Cañada, Carretera Teotitlán – San Antonio Nanahutipan Km 1.7 s/n. Paraje Titlacuatitla, 68540, Teotitlán de Flores Magón, Oaxaca, México*

(*Received 22 November 2011; final version received 9 May 2012*)

A piecewise linear algorithm for predicting silicon etch rates in fluorine-based plasmas is shown. Discrete experimental data of pressure and RF power in reactive ion etching are used to construct a set of local two-dimensional etching functions that serve as a basis for computing numerical solutions (pressure and power values for a specific predicted silicon etch rate). It must be pointed out that, although the algorithm scans the entire data domain, a testing procedure is applied to ensure that the computing task will be invoked only when a solution exists, and otherwise it will be discarded (this avoids brute force methods). In the last step of the algorithm, all solutions are collected and interpolated to construct a *solution path*. In order to verify the match between the experimental etching results and numerical predictions, the algorithm has been coded and tested using Maple® Release 13.0, showing a successful validation with a difference between experimental data and computed numerical solutions as low as 1% for SF_6, and 4% for SF_6/O_2 in the best case and a root-mean squared error of 0.03.

Keywords: silicon etching; piecewise linear; algorithm

1. Introduction

Plasma-based etching of silicon is a very important step in integrated circuits and micro-electro-mechanical systems fabrication. However, the plasma process involves many operating conditions and as a consequence, it exhibits complex behavior. Even so, silicon etching is still based on empirical data where the process characterization is carried out with the variation of plasma parameters as RF power, work pressure, DC self-bias, and type and gas flow. In this way, the best result for a particular application is found. Predicting any behavior in a plasma process must be an important goal in any laboratory, because better experiments can be designed and optimized, as well as reducing time and process costs; therefore, a prediction algorithm is a very useful tool. Computational models, most of them based on neural networks and wavelets, are widely used in developing etch models in order to understand and forecast plasma processes. Successful results have been obtained to determine etching characteristics as a function of plasma parameters using, for example, identification algorithms (Meng *et al*. 1999), adaptively trained neural network (Choi and Kim 2000), back propagation neural network (Kim *et al*. 2002a, 2004a, Kim and Kwon 2003, Kim and Kim 2005), discrete wavelet transformation (Kim *et al*. 2003a, 2003b, 2008, Kim and Kim 2007a, 2007b), generalized regression neural network (Kim *et al*. 2003c, 2004b, 2004c, 2005a, 2005b, Kim and Lee 2004a, 2004b, 2005), adaptive network fuzzy inference system (Kim *et al*. 2004a), classification-based neural network (Kim and Kim 2004), radial basis function network and genetic algorithm (Han *et al*. 2005), multivariable real-time intelligent control neural network (Tudoroiu *et al*. 2006), feedforward neural network (Xia *et al*. 2010), or using a comparison among several neural networks models and wavelets (Lee *et al*. 2003, Kim *et al*. 2003d, 2003e). In some cases, an additional *in situ* technique has been

*Corresponding author. Email: vicjimenez@uv.mx

© 2013 The Chinese Institute of Engineers

used to improve the model, for example, optical emission spectroscopy (Kim *et al*. 2002b, 2005c, Kim and Kwon 2009) or X-ray photoelectron spectroscopy (Kim and Kim 2007c). In this work, we show that a piecewise linear (PWL) algorithm is one alternative strategy to predict etch data, based on the relationship between controllable plasma parameters.

In this sense, considering that most of the reported publications about the etching rate estimation show an approach based on neural networks, it is important to highlight the advantages that PWL exhibits over the neural network implementation. First, neural networks need training to operate, making them computationally expensive and time consuming. In contrast, in PWL only a finite and reduced set of input/output measurements is needed. Second, the algorithmic implementation of neural networks is composed of multiple interconnected layers resulting in a more complex structure compared with PWL. Third, the component functions in PWL are easily tractable due to its linear nature, while in neural networks the inclusion of nonlinear activation functions increases complexity. Finally, unlike several neural network algorithmic proposals, where only one solution can be computed, the PWL algorithm has proven to be able to find not only one but also multiple solutions to achieve one specific silicon etching rate.

The proposed PWL algorithm emerges from two kinds of analyses: numerical and geometrical. From a numerical perspective, the problem under study is overcome by finding the solutions of the nonlinear equation:

$$F(\boldsymbol{X}) - k = 0 \tag{1}$$

where $F(\boldsymbol{X})$ denotes the local PWL function that models the experimental process, etch rate of silicon in our case, k is a specific output datum value (predicted etch rate of silicon, $F(\boldsymbol{X}) = k$), and $\boldsymbol{X} \in \boldsymbol{R}^2$ indicates the set of solutions (controllable plasma parameters) to satisfy Equation (1). From a geometrical point of view, the solutions are derived from the intersection between two curves: the $\boldsymbol{R}^2$ response surface that describes the experimental process and the plane defined by the constant k. These two analyses are related to each other and they have been combined as an integrated methodology denoted as simplicial because the $\boldsymbol{R}^2$ curve of data is considered to be always defined over the so-called simplicial domain (Chien and Kuh 1977).

It is important to note that, up to the moment, no work has been reported, using a PWL analysis to determine the plasma etch rate of silicon for semiconductor manufacturing.

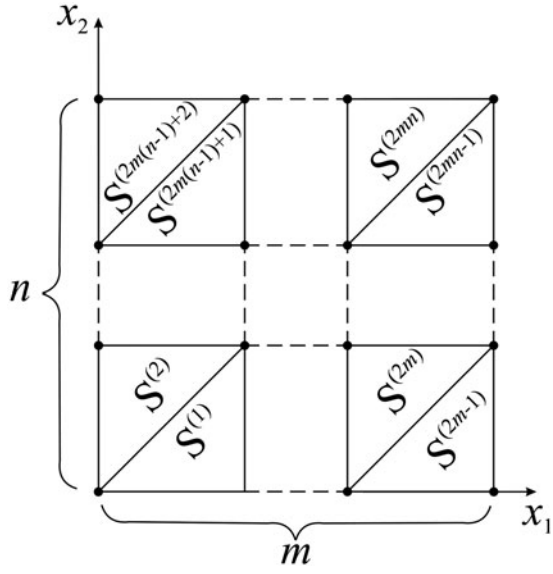

Figure 1. A two-dimensional domain divided into regular simplices.

2. PWL model description

Consider a two-dimensional $(m \times n)$ domain divided into $(2 \times m \times n)$ equally sized triangular regions as illustrated in Figure 1.

Each region, denoted as simplex $S^{(j)}$ (for $j = 1, 2, \ldots, 2mn$), is defined by the convex combination of its vertices as follows:

$$S(x_1, x_2) = \left\{ \boldsymbol{X} | \boldsymbol{X} = [x_1, x_2]^T = \sum_{i=1}^{3} \mu_i v_i \right\}, \quad \text{with } \sum_{i=1}^{3} \mu_i = 1. \tag{2}$$

The μ_i terms (for $i = \{1, 2, 3\}$) are weighting parameters which are related with the internal position of $\boldsymbol{X}$ into the jth simplex ($j = 1, 2, \ldots, 2mn$), and v_is are the unitary vertices of the simplex where $\boldsymbol{X}$ is located. If one value is associated with each vertex, then it is possible to define a local (linear) function $f^{(j)}(\boldsymbol{X}) = a^{(j)}\boldsymbol{X} + b^{(j)}$ for each jth simplex (Julian 1999, Julian and Agamennoni 1999, Julian *et al*. 2000). The collection of local functions makes it possible to define (globally) a PWL function $F(\boldsymbol{X}) = \cup_{j=1}^{2mn} f^{(j)}(\boldsymbol{X})$ over the simplicial domain $S(\boldsymbol{X}) = \cup_{j=1}^{2mn} S^{(j)}$. Figure 2 illustrates this constructive strategy for a (2×2) domain.

Each triangular image over the $\boldsymbol{R}^2$ domain is defined by the local function:

$$f^{(j)}(\boldsymbol{X}) = \sum_{i=1}^{3} \mu_i c_i \tag{3}$$

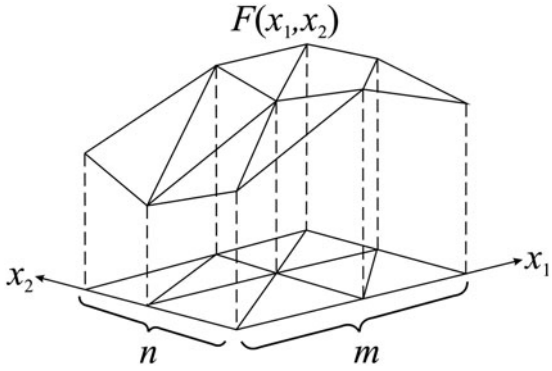

Figure 2. A constructive strategy for a two-dimensional function in a (2×2) domain.

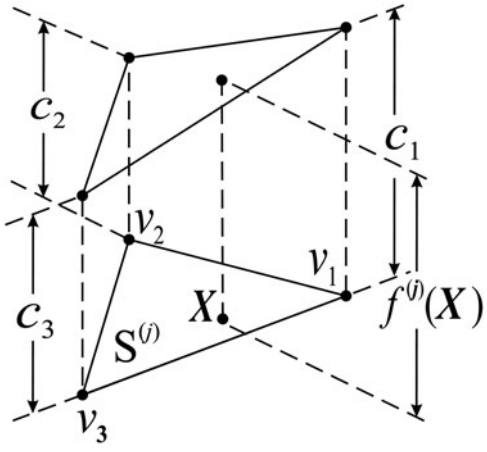

Figure 3. Parameters of a simplicial function in a two-dimensional domain.

where $\boldsymbol{X} = [x_1, x_2]^T$ is an arbitrary point which belongs to the $\boldsymbol{R}^2$ domain and c_is are the values of the function at the vertices of the simplices. In order to clarify the meaning of Equation (3), Figure 3 illustrates the geometrical representation of parameters for a jth simplex.

3. Approaching the problem

In order to determine the set of $\boldsymbol{X}$ solutions, hereafter denominated as *solution path*, for a given function value k, a particular problem of two dimensions, as depicted in Figure 4, is considered.

From a geometrical point of view, this problem can be seen as the intersection between the $F(x_1, x_2)$ response surface and the plane k. The projection of $F(\boldsymbol{X}) = k$ into the simplicial domain $\boldsymbol{X}$ represents the *solution path* for this problem.

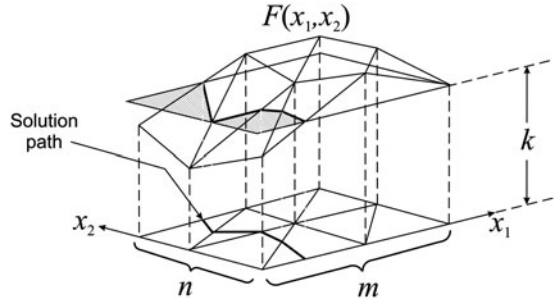

Figure 4. X solution path for a two-dimensional curve.

4. Equations for computing the solution path

All solutions, for the nonlinear equation $F(\boldsymbol{X}) - k = 0$, are collected into a one-dimensional *solution path* as a PWL curve over the $\boldsymbol{X}$-domain (Allgower and Georg 1980, Allgower and Schmidt 1985, Allgower and Gnutzmann 1987). Due to the equally grid-sized partition domain, each linear segment of the *solution path* can be described by two (x_1, x_2) coordinates at every simplex. Such coordinates can be computed using the one-dimensional form of Equation (2) obtained as follows:

First, Equations (2) and (3) are rewritten into the matrix system of Equation (4):

$$\begin{bmatrix} f^{(j)}(x) \\ 1 \end{bmatrix} = \begin{bmatrix} c_{j-1} & c_j \\ 1 & 1 \end{bmatrix} \begin{bmatrix} \mu_1 \\ \mu_2 \end{bmatrix}. \tag{4}$$

Then, after solving for μ_1 and μ_2, one obtains

$$\mu_1 = \frac{f^{(j)}(x) - c_{j+1}}{c_j - c_{j+1}}, \quad \mu_2 = \frac{c_j - f^{(j)}(x)}{c_j - c_{j+1}}. \tag{5}$$

After that, the one-dimensional form of Equation (2) can be expressed as

$$x = \frac{v_{j+1}\left[f^{(j)}(x) - c_j\right] - v_j\left[f^{(j)}(x) - c_{j+1}\right]}{c_{j+1} - c_j}. \tag{6}$$

Finally, $f^{(j)}(\boldsymbol{X})$ is substituted for k, and x is denoted by x_k which allows the recasting of Equation (6) as follows:

$$x_k = \frac{v_{j+1}\left[k - c_j\right] - v_j\left[k - c_{j+1}\right]}{c_{j+1} - c_j}. \tag{7}$$

The above equation can be used to determine the breakpoint coordinates for the jth linear segment of the *solution path*. It must be observed that Equation (7) only requires two vertices (v_j, v_{j+1}) and the value of function at those vertices (c_j, c_{j+1}) as input variables. Figure 5 shows the geometrical meaning of Equation (7) for a jth constitutive segment.

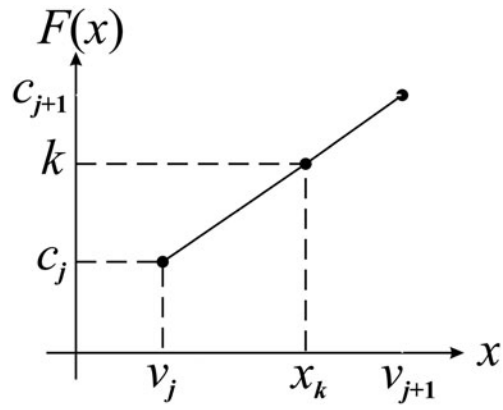

Figure 5. Simplicial parameters of a constitutive linear segment.

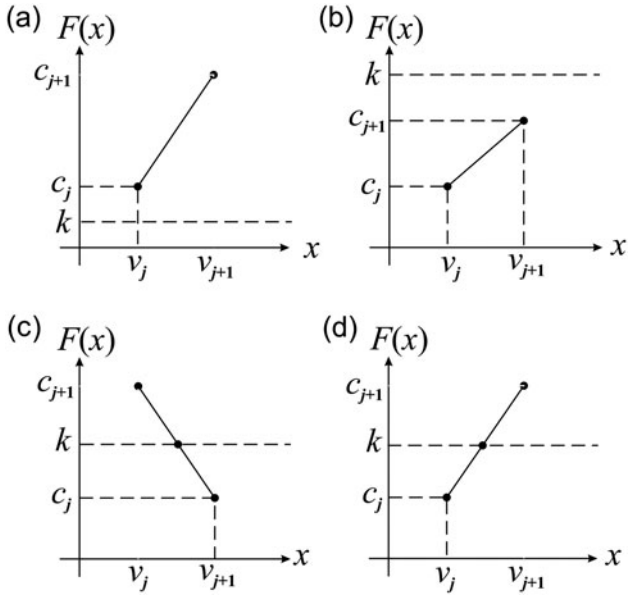

Figure 6. Four possible cases to test the existence of a solution.

Because it is clear that not all simplices are host to a solution, then an additional procedure to discard empty-solution simplices is required. The discarding simplex procedure takes into account the four possibilities shown in Figure 6.

In Figure 6, cases (a) and (b) illustrate when a solution does not exist, and cases (c) and (d) when a solution exists. The existence of a solution is related by a test parameter τ given by

$$\tau = \left| t_j + t_{j+1} \right| \tag{8}$$

Table 1. XOR logical behavior for the test parameter (τ).

t_j	t_{j+1}	$\tau = \lvert t_j + t_{j+1} \rvert$
−1	−1	2
−1	1	0
1	−1	0
1	1	2

with

$$t_j = \operatorname{sgn}(k - c_j), \quad t_{j+1} = \operatorname{sgn}(k - c_{j+1}), \tag{9}$$

and sgn(·) described the signum function defined as

$$\operatorname{sgn}(a) = \begin{cases} +1 & \text{if } a \geq 0 \\ -1 & \text{if } a < 0 \end{cases}. \tag{10}$$

Table 1 summarizes the τ value for the cases of Figure 6.

It is important to note that when $\tau = 0$ there is a solution, and otherwise there is no solution. In fact, this is the testing condition to discard the empty-solution intervals and select specifically interval segments where a solution exists. As an additional observation, it can be seen that Table 1 exposes a hypothetical *XOR* logical behavior.

5. The PWL algorithm

Let the behavior of a two-dimensional system be described by a finite set of $(m \times n)$ input ordered pairs and their corresponding $(m \times n)$ discrete $F(\boldsymbol{X})$ outputs. The algorithm for computing the solution path that satisfies $F(\boldsymbol{X}) - k = 0$ is summarized as follows:

Step 1: *Define a matrix with the $F(\boldsymbol{X})$ output data and deal with their elements as discrete values belonging to a PWL function.* Due to the fact that a set of PWL functions $f^{(j)}(x_1, x_2)$ is defined over an $(m \times n)$-simplicial domain, the global PWL function $F(\boldsymbol{X}) = \cup_{j=1}^{2mn} f^{(j)}(\boldsymbol{X})$ is only described by a set of discrete parameters: $\{(m+1) \times (n+1)\}$ vertices and $\{(m+1) \times (n+1)\}$ values at vertices. These parameters are implicitly defined in an $(m \times n)$ $\boldsymbol{C}$-matrix as follows:

$$\boldsymbol{C} = \begin{bmatrix} c_{0,0} & c_{0,1} & \cdots & c_{0,n-1} & c_{0,n} \\ c_{1,1} & c_{1,2} & & c_{1,n-1} & c_{1,n} \\ \cdot & & & & \cdot \\ \cdot & & & & \cdot \\ \cdot & & & & \cdot \\ c_{m-1,1} & c_{m-1,2} & & c_{m-1,n-1} & c_{m-1,n} \\ c_{m,1} & c_{m,2} & \cdots & c_{m,n-1} & c_{m,n} \end{bmatrix} \tag{11}$$

Step 2: *Compute solutions for the vertical sweep*. The elements of ***C***-matrix are addressed in order column by column. This means scanning the ***X*** domain for *i*th value of x_1 ($i = 0, 1, \ldots, m$). This step has been denoted as 'vertical sweep' because every *i*th substitution transforms the original two-dimensional function $F(\boldsymbol{X})$ into a one-dimensional function which can be seen like a vertical cutoff of $F(\boldsymbol{X}) = F(x_1, x_2)$ at $x_1 = i$. In this step, solutions for $F(i, x_2) - k = 0$ are computed through Equation (7), but the existence of a solution at each *i*th value is previously verified by Equations (8) and (9). If a solution exists ($\tau = 0$), then Equation (7) is applied and the x_kth solution is stored in memory; otherwise, the application of Equation (7) is discarded. This procedure is iteratively repeated for $i = 0, 1, \ldots, m$ in each column of the ***C***-matrix.

Step 3: *Compute solutions for the horizontal sweep*. The elements of the ***C***-matrix are addressed in order, row by row. In the same way as the previous step, every *i*th substitution transforms the original two-dimensional function into a one-dimensional function like a horizontal cutoff of $F(\boldsymbol{X}) = F(x_1, x_2)$ at $x_2 = i$. Similarly, as in step 2, the existence of the x_kth solution is verified before applying Equation (7), if $\tau = 0$ then solutions for $F(x_1, i) - k = 0$ are computed and stored in memory. This procedure is iteratively repeated for $i = 0, 1, \ldots, m$ in each row of the ***C***-matrix.

Step 4: *Compute solutions for the diagonal sweep*. The elements of the ***C***-matrix are addressed by following a diagonal order. From a geometrical perspective, it means the scanning of ***X***-domain along the $x_2 = x_1 + j$ line with $j = \{1, 2, \ldots, n-1\} \cup \{2, 3, \ldots, m-1\}$. In the same way as done in the two previous steps, if $\tau = 0$ is fulfilled, then solutions for $F(x_1, x_1 + j) - k = 0$ are computed through Equation (7) and stored in memory.

Step 5: *Collect all solutions*. A linear interpolation of the numerical solutions which are stored in memory represents the *solution path* for Equation (1).

6. Experimental procedure

Silicon etching experiments were carried out with *n* type and (100) orientation monocrystalline substrates. Wafers were patterned by a MA-P215 photo resist mask. Samples of approximately 0.5 cm^2 were etched on a Reactive Ion Etching-driven (13.56 MHz) plasma reactor, using SF_6 gas and SF_6/O_2 gas mixture. The etching parameters were gas pressures of 50, 75, 100, 125, 150, and 175 mTorr, RF powers of 50, 75, 100, 125, 150, and 175 W. Gas flows of 50 sccm and 50 sccm/5 sccm for SF_6 and SF_6/O_2, respectively. Etching time was fixed at 5 min. Etch depths were measured by a Wyko NT1100 Optical Profiling System; 36 data were used to characterize the silicon etching with SF_6, and 36 data to characterize the silicon etching with SF_6/O_2 processes. The input signals were the RF power and the pressure, and the output signal was the etch rate.

7. Experimental verification

Experimental results for silicon etching using SF_6 gas are shown in Table 2, where the characteristic nonlinear behavior in plasma etching processes can be observed, even when a simple chemistry such as SF_6 plasma is used.

The etch rate increases as the power increases, both ions and neutral reactants increase with power, promoting higher etch rates. However, the etch rate has an opposite behavior with pressure. At lower pressure, ion bombardment energy rises and the density of neutral reactants decreases, resulting in higher etch rates with a dominant physical mechanism of etching. At higher pressure, ion energy decreases, and the density of neutral reactants increases, promoting a chemical etching with lower etch rate. In Table 3, experimental results using SF_6/O_2 gas mixture are presented.

Nonlinear behavior is also observed, and etch rates increase when only SF_6 is used. SF_6/O_2 gas mixtures are used in order to promote vertical profiles by the formation of a passivating layer on the surface. When O_2 is added the concentration of F radicals increases, promoting a higher etch rate of silicon. In this case, the highest etch rates are obtained for high pressure and high power. Under our conditions, the thin passivating layer could be easily removed by the high concentration of F radicals with low contribution of ion bombardment giving faster etching results. The simplicial algorithm developed in Section 5 is now applied to determine the required adjustment of parameters, RF power, and pressure, in order to achieve a specific value of etch rate for SF_6 and SF_6/O_2 plasmas. Graphical view of the experimental data for Table 2 is given by the PWL surface response depicted in Figures 7 and 8.

As experimental results show, the etch rate increases with higher power and lower pressure. The algorithm described in Section 5 is coded in Maple® Release 13.0 and tested by providing the numerical silicon etch prediction as input (*k* value) in order to compute power and pressure values (***X*** solution) as output. After that, the computed values of power and pressure are used in a silicon etching process (with SF_6 as reactive gas) in order to compare the match between the experimental etching result and its numerical

Table 2. Experimental data for the algorithm design, SF_6 plasma.

SF_6 – 50 sccm					
Pressure (W)	RF power (mTorr)	Silicon etch rate (nm/min)	Pressure (W)	RF power (mTorr)	Silicon etch rate (nm/min)
50	50	92	125	50	86
	75	142		75	112
	100	180		100	156
	125	228		125	184
	150	252		150	210
	175	308		175	216
75	50	106	150	50	52
	75	128		75	110
	100	172		100	162
	125	196		125	146
	150	206		150	196
	175	262		175	222
100	50	102	175	50	56
	75	106		75	84
	100	96		100	114
	125	188		125	156
	150	234		150	164
	175	244		175	184

Table 3. Experimental data for the algorithm design, SF_6/O_2 plasma.

SF_6/O_2 – 50 sccm/5 sccm					
Pressure (W)	RF power (mTorr)	Silicon etch rate (nm/min)	Pressure (W)	RF power (mTorr)	Silicon etch rate (nm/min)
50	50	130	125	50	110
	75	150		75	170
	100	240		100	236
	125	260		125	302
	150	272		150	380
	175	350		175	420
75	50	100	150	50	64
	75	154		75	174
	100	180		100	212
	125	170		125	320
	150	260		150	334
	175	330		175	392
100	50	100	175	50	58
	75	176		75	150
	100	240		100	176
	125	310		125	260
	150	340		150	274
	175	370		175	326

prediction. Table 4 shows random data of etch prediction (INPUT), the corresponding power and pressure values computed by the PWL algorithm (OUTPUT), and the experimental silicon etching that results denoted as specific processes (*A–J*).

As can be observed, process *G* appeared to be the best approximation with an error of 1%, while process *C* had an error of 23%. In spite of this value, this can be considered a good approximation. It must be noted that each numerical prediction belongs to a specific

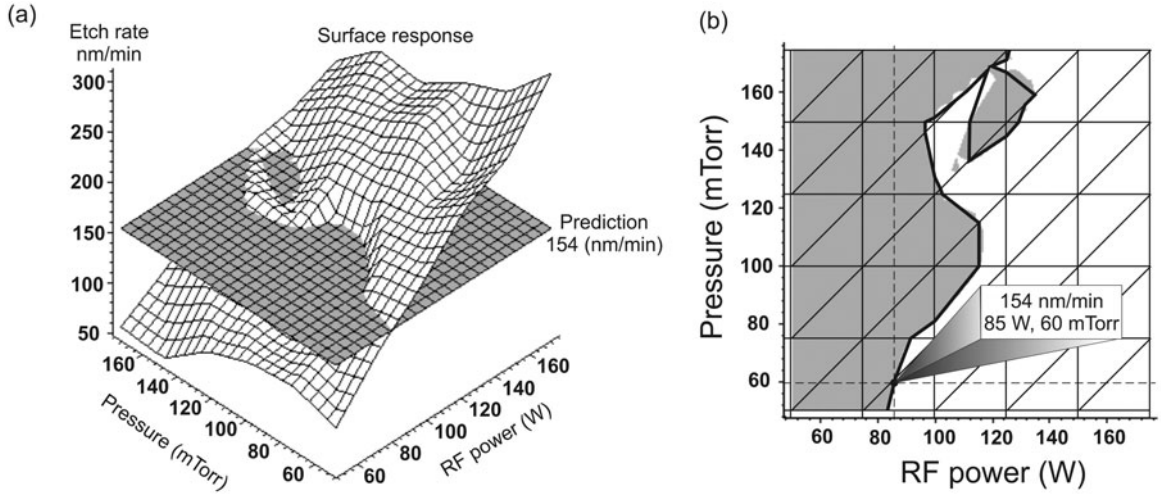

Figure 7. Solution path for an etch rate of 154 nm/min in SF_6 plasma: (a) surface response and predicted value intersection and (b) process G (85 W-60 mTorr) in the *solution path*.

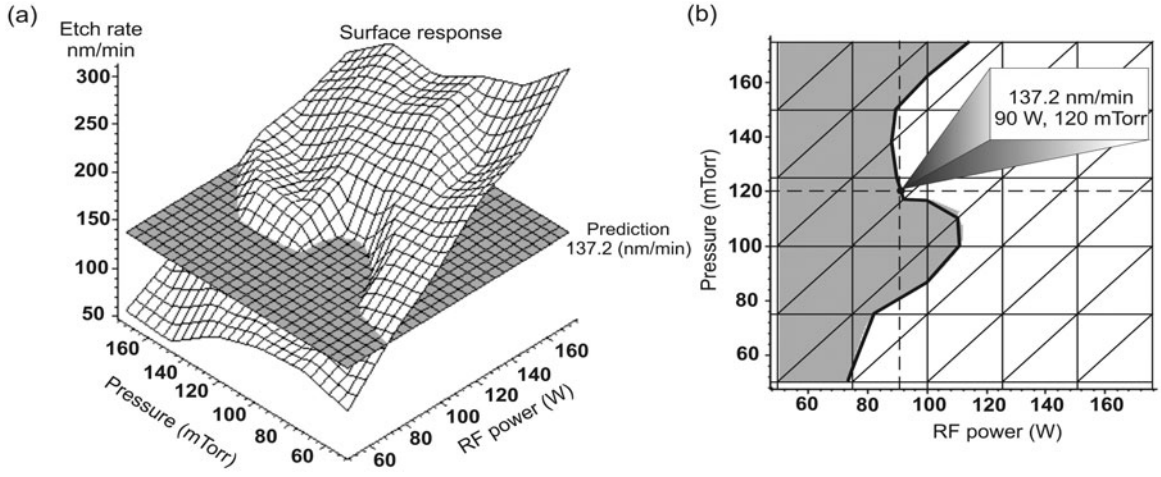

Figure 8. Solution path for an etch rate of 137.2 nm/min in SF_6 plasma: (a) surface response and predicted value intersection and (b) process H (90 W-120 mTorr) in the *solution path*.

Table 4. Algorithm validation with experimental results for etching with SF_6.

Input	Output		Experimental results	
Silicon etch rate (nm/min) Numerical prediction	RF power (W)	Pressure (mTorr)	Silicon etch rate (nm/min) Experimental data	Process
95.6	50	110	91	*A*
107.6	55	70	98	*B*
114.8	60	75	149	*C*
110.4	70	90	134	*D*
123.6	75	80	144	*E*
142.4	80	65	160	*F*
154	85	60	153	*G*
137.2	90	120	140	*H*
199.2	110	50	210	*I*
192.8	125	85	222	*J*

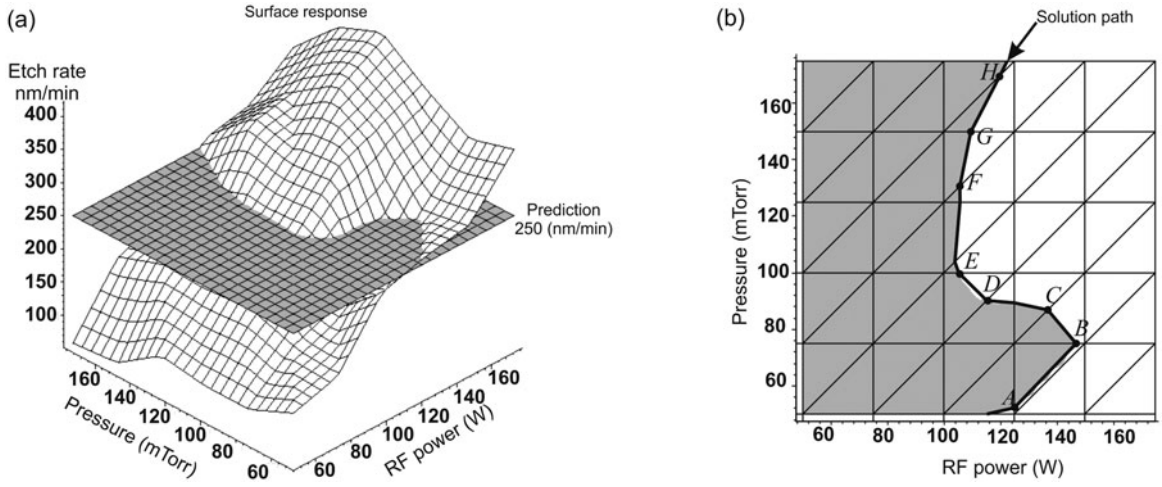

Figure 9. Solution path for an etch rate of 250 nm/min in SF_6/O_2 plasma: (a) surface response and predicted value intersection and (b) eight possible solutions (processes) in the *solution path* were found.

Table 5. Algorithm validation with experimental results for etching with SF_6/O_2.

Input	Output		Experimental results	
Silicon etch rate (nm/min) Numerical prediction	Pressure (mTorr)	RF power (W)	Silicon etch rate (nm/min) Experimental data	Process
250	53	110	230	*A*
	75	70	228	*B*
	85	75	200	*C*
	89	90	240	*D*
	100	80	230	*E*
	126	65	196	*F*
	150	60	224	*G*
	170	120	230	*H*

solution path that results from the interpolation of the numerical solutions. Solution paths for processes *G* and *H* are depicted in Figures 7 and 8, respectively. Graphical view of the experimental data for Table 3 is given by the PWL surface response shown in Figure 9.

The algorithm is coded and tested by providing a singular numerical silicon etch prediction as input (k value) in order to compute several power and pressure values ($\boldsymbol{X}$ solution) as output for a unique input. The computed values of power and pressure are used in silicon etching processes (in this case, for SF_6/O_2 plasma) in order to compare the match between experimental etching results and their numerical predictions. Table 5 shows the unique data of etch prediction (INPUT), the corresponding power and pressure values computed by the PWL algorithm (OUTPUT), and the experimental silicon etching that results denoted as specific processes (*A–H*). The best obtained approximation showed an error of 4% (process *D*). Solution path for processes *A–H* are depicted in Figure 9.

8. Conclusions

In this article, the problem of predicting silicon etch rates by a PWL algorithm was approached. The algorithm was able to provide a *solution path* containing RF power and pressure values that could fulfill the silicon etch prediction. In order to verify the effectiveness of the computed values for power and pressure, experimental processes of plasma etching of silicon with SF_6 gas and SF_6/O_2 gas mixture were performed, achieving in the best case, an error of 1% between the algorithm prediction and the experimental result for SF_6 and 4% for SF_6/O_2. These results showed that in

the presence of a passivation process on the surface, a higher error could be considered. However, good approximations for both cases were obtained. In conclusion, PWL showed itself to be a useful computational tool to predict experimental results in semiconductor manufacturing.

Acknowledgments

This research was partially supported by CB-CONACyT project 102669 of 'Instituto Tecnológico Superior de Xalapa', Veracruz-Mexico, and CONACyT projects 42906 and 59890 of the National Institute for Astrophysics, Optics and Electronics, Puebla-Mexico.

Nomenclature

$F(X)R^2$	PWL function
k	predicted output value
m	number of discrete data for x_1
n	number of discrete data for x_2
$S^{(j)}$	jth simplex
v	vertex of simplex
c	value of function at vertex
μ	weighting parameter
τ	parameter for testing
$\boldsymbol{C}$	data matrix

References

Allgower, E.L. and Georg, K., 1980. Simplicial and continuation methods for approximating fixed points and solutions to systems of equations. *SIAM review*, 22 (1), 28–85.

Allgower, E.L. and Gnutzmann, S., 1987. An algorithm for piecewise linear approximation of implicitly defined two-dimensional surfaces. *SIAM journal on numerical analysis*, 24 (2), 452–469.

Allgower, E.L. and Schmidt, P.H., 1985. An Algorithm for piecewise-linear approximation of an implicitly defined manifold. *SIAM journal on numerical analysis*, 22 (2), 322–346.

Chien, M. and Kuh, E., 1977. Solving nonlinear resistive networks using piecewise-linear analysis and simplicial subdivision. *IEEE transactions on circuits and systems*, 24 (6), 305–317.

Choi, M.K. and Kim, H.M., 2000. Process control to improve yield in the plasma etching process using an adaptively trained neural network. *JSME international journal series C*, 43 (3), 594–602.

Han, D., *et al*., 2005. Modelling of plasma etching process using radial basis function network and genetic algorithm. *Vacuum*, 79 (3), 140–147.

Julian, P., 1999. *A high level canonical piecewise linear representation: theory and applications*. Thesis (PhD). Universidad Nacional del Sur, Bahía Blanca, Argentina.

Julian, P. and Agamennoni, O., 1999. High-level canonical piecewise linear representation using a simplicial partition. *IEEE transactions on circuits and systems I*, 46 (4), 463–480.

Julian, P., Desagues, A., and D'Amico, B., 2000. Orthonormal high-level canonical PWL functions with applications to model reduction. *IEEE transactions on circuits and systems I*, 47 (5), 702–712.

Kim, B., Choi, W.S., and Lim, M.T., 2003a. Wavelet monitoring of plasma etching. *Journal of vacuum science and technology B*, 21 (6), 2329–2333.

Kim, B. and Kim, S., 2004. Prediction of plasma etching using a classification-based neural network. *Journal of the electrochemical society*, 151 (9), C585–C589.

Kim, B. and Kim, S., 2005. Diagnosis of plasma processing equipment using neural network recognition of wavelet-filtered impedance matching. *Microelectronic engineering*, 82 (1), 44–52.

Kim, B. and Kim, W.S., 2007a. Wavelet monitoring of spatial surface roughness for plasma diagnosis. *Microelectronic engineering*, 84 (12), 2810–2816.

Kim, B. and Kim, W.S., 2007b. Wavelet uniformity of plasma-processed surface roughness. *Vacuum*, 81 (5), 649–655.

Kim, B. and Kim, W.S., 2007c. Partial x-ray photoelectron spectroscopy to constructing neural network model of plasma etching surface. *Microelectronic engineering*, 84 (4), 584–589.

Kim, B., Kim, S., and Kim, K., 2003b. Modeling of plasma etching using a generalized regression neural network. *Vacuum*, 71 (4), 497–503.

Kim, B., Kim, S., and Lim, M.T., 2003c. Wavelet-based uniformity of plasma etching surface. *IEEE transactions on plasma science*, 31 (6), 1313–1316.

Kim, B., Kim, D.W., and Park, G.T., 2003d. Prediction of plasma etching using a polynomial neural network. *IEEE transactions on plasma science*, 31 (6), 1330–1336.

Kim, D.W., Kim, B.W., and Park, G.T., 2004a. A plasma-etching process modeling via a polynomial neural network. *ETRI journal*, 26 (4), 297–306.

Kim, B., Kong, S., and Lee, B.T., 2002a. Modeling SiC etching in C_2F_6/O_2 inductively coupled plasma using neural networks. *Journal of vacuum science and technology A*, 20 (1), 146–152.

Kim, B. and Kwon, K.H., 2003. Qualitative modeling of silica plasma etching using neural network. *Journal of applied physics*, 93 (1), 76–82.

Kim, B. and Kwon, M., 2009. Prediction of plasma etch process by using actinometry-based optical emission spectroscopy data and neural network. *Journal of materials processing technology*, 209 (5), 2620–2626.

Kim, B. and Lee, D.W., 2004a. Prediction of SiC etching in a NF_3/CH_4 plasma using neural network. *Journal of vacuum science and technology A*, 22 (6), 2517–2522.

Kim, B. and Lee, D.W., 2004b. Prediction of plasma etching using a randomized generalized regression neural network. *Vacuum*, 76 (1), 37–43.

Kim, B. and Lee, B.T., 2005. Prediction of silicon oxynitride plasma etching using a generalized regression neural network. *Journal of applied physics*, 98 (3), 034912-1–034912-6.

Kim, B., Lee, D.W., and Kwon, K.H., 2004b. Prediction of etch microtrenching using a neural network. *Journal of applied physics*, 96 (7), 3612–3616.

Kim, B., Lee, B.T., and Lee, K.K., 2005a. On the use of a neural network to characterize the plasma etching of SiON thin films. *Journal of materials science*, 16 (10), 673–679.

Kim, B., Park, K.Y., and Han, D., 2004c. Modelling plasma etching of Al thin films using neural network. *Surface engineering*, 20 (6), 454–458.

Kim, B., Uh, H.S., and Kim, D., 2008. Ex-situ plasma diagnosis by combining scanning electron microscope, wavelet, and neural network. *Materials science in semiconductor processing*, 11 (3), 87–93.

Kim, B., *et al*., 2002b. Modeling oxide etching in a magnetically enhanced reactive ion plasma using neural networks. *Journal of vacuum science and technology B*, 20 (5), 2113–2119.

Kim, B., *et al*., 2003e. Modeling etch rate and uniformity of oxide via etching in a CHF_3/CF_4 plasma using neural networks. *Thin solid films*, 426 (1), 8–15.

Kim, B., *et al*., 2005b. Modeling a sidewall bottom etching using a neural network. *Journal of the Korean physical society*, 46 (6), 1365–1370.

Kim, B., *et al*., 2005c. Use of a neural network to model SiC etching in a NF3 inductively coupled plasma. *Modelling and simulation in materials science and engineering*, 13 (8), 1267–1277.

Lee, H.S., *et al*., 2003. Qualitative interpretation of etch profile nonuniformity using a wavelet and neural network. *Journal of the Korean physical society*, 43 (5), 817–821.

Meng, H., *et al*., 1999. Modelling and control of plasma etching processes in the semiconductor industry. *Computers and industrial engineering*, 37 (1), 367–370.

Tudoroiu, N., Patel, R., and Khorasani, K., 2006. Neural network based control strategies for improving plasma characteristics in reactive ion etching. *Neurocomputing*, 69 (7), 786–802.

Xia, J., Rusli, H., and Kumta, A.S., 2010. Feedforward neural network trained by BFGS algorithm for modeling plasma etching of silicon carbide. *IEEE transactions on plasma science*, 38 (2), 142–148.